Diverse Structural and Magnetic Properties of Differently Prepared MnAs Nanoparticles

Peng Tian,[†] Yanhua Zhang,[‡] Keerthi Senevirathne,[‡] Stephanie L. Brock,[‡,*] Ambesh Dixit,[§] Gavin Lawes,[§] and Simon J. L. Billinge[⊥,∥,*]

[†]Department of Physics and Astronomy, Michigan State University, East Lansing, Michigan 48824, United States, [‡]Department of Chemistry, Wayne State University, Detroit, Michigan 48202, United States, [§]Department of Physics, Wayne State University, Detroit, Michigan 48201, United States, [⊥]Department of Applied Physics and Applied Mathematics, Columbia University, New York, New York 10027, United States, and [∥]Department of Condensed Matter Physics and Materials Science, Brookhaven National Laboratory, Upton, New York 11973, United States

ABSTRACT Discrete nanoparticles of MnAs with distinct magnetostructural properties have been prepared by small modifications of solution-phase arrested precipitation reactions. Rietveld and X-ray atomic pair distribution function based approaches were used to explore the evolution of the structure of the samples with temperature, and these data were compared to the magnetic response measured with ac susceptibility. Relative to a bulk standard, one type of MnAs nanoparticles was found to demonstrate similar but smaller structural transitions and corresponding magnetic changes. However, both magnetic and structural transitions in the second type of nanoparticles are strongly suppressed.

KEYWORDS: MnAs · structure · magnetic · PDF · nanoparticle

MnAs has been noted as an attractive candidate for information storage and energy applications due to its interesting magnetic and structural properties.[1−3] Bulk MnAs has a magnetostructural phase transition in which a first-order magnetic transition occurs from a high-spin ferromagnetic to a low-spin paramagnetic state with a concomitant structural transition from the hexagonal α phase (NiAs-type) to the orthorhombic β phase (MnP-type).[4] The transition occurs at 315 K upon warming. At a higher temperature, 400 K, a reentrant second-order phase transition takes place back to the α phase, but the high-spin state is now paramagnetic. This sequence of transitions is shown in Figure 1.

In studies on bulk MnAs, scientists observed that the structural transition can be driven by the application of a magnetic field,[1] which confirms that the coupling between the magnetic transition and structural transition is strong. These properties result in a tunable magnetocaloric effect in bulk MnAs that could be applied in microelectronic circuit[5,6] applications. A number of theoretical studies[4,7] have discussed the correlation between structure and magnetism, although there is no clear understanding of the details of the relationship.

Compared to bulk materials, nanoscale materials exhibit size and shape tunable physical properties such as electronic, magnetic, and catalytic properties. Research on nanoscale MnAs has been largely focused on epitaxially grown MnAs particles or disks on semiconducting thin films[8] or nanowires.[9] Such nanoscale MnAs is a promising material for thermally assisted magnetic recording.[8] However, these epitaxial structures are subject to external pressure due to lattice strain from the substrate, resulting in significant shifts in the magnetostructural transition temperatures. Recently, a method for preparing MnAs as discrete unsupported nanoparticles[10] enables the effect of size on the first-order transition to be probed in the absence of external stress. Particles of 9−23 nm were prepared in solution by reaction of dimanganesedecacarbonyl ($Mn_2(CO)_{10}$) and triphenylarsine oxide ($(C_6H_5)_3As{=}O$) in coordinating solvents at temperatures ranging from 523 to 603 K. Intriguingly, small changes in the synthetic method led to two distinctly different products, as detected by powder X-ray diffraction conducted at room temperature. Notably, in one case, the metastable β structure, rather than the thermodynamic α structure, was observed. Despite the presence of a magnetic transition consistent with the magnetostructural transformation in bulk MnAs, no evidence was observed of a corresponding structural transition in temperature-dependent powder X-ray diffraction measurements for either material.[10]

Here we perform a detailed structural evaluation of the two types of MnAs

* Address correspondence to sbrock@chem.wayne.edu; sb2896@columbia.edu.

Received for review January 3, 2011 and accepted March 2, 2011.

Published online March 02, 2011
10.1021/nn200020r

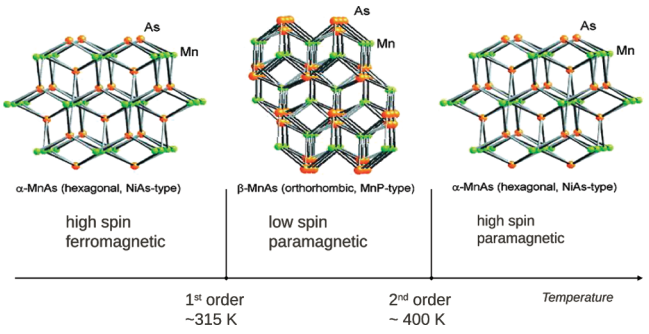

Figure 1. Schematic diagram of the structures and transitions in bulk MnAs.

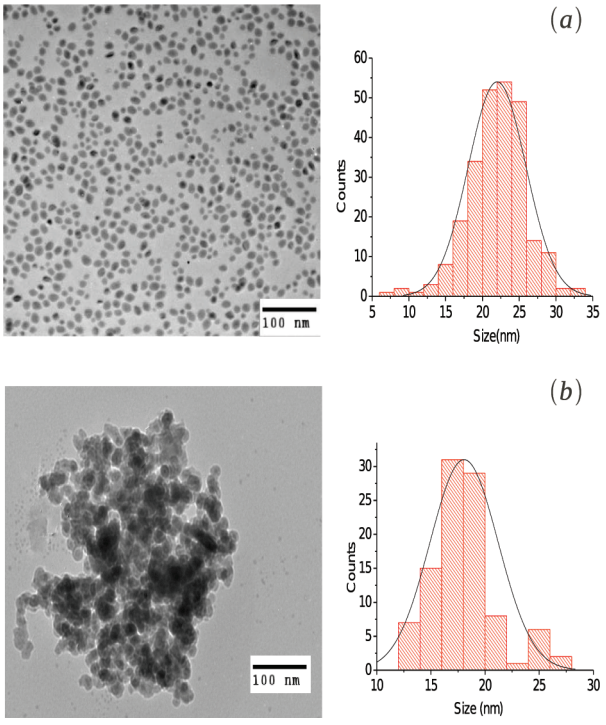

Figure 2. TEM images and particle size distributions of type-A (a) and type-B (b) MnAs nanoparticles.

nanoparticles using an advanced nanostructure determination method, the atomic pair distribution function (PDF) technique[11−14] as a function of temperature in the region of the expected magnetostructural transition. The obsesrvations from these data are correlated with ac magnetic susceptibility data acquired over the same temperature range. We show that nanoparticles synthesized using one approach behave like the bulk, albeit at a reduced level. Nanoparticles synthesized by the other method appear to be kinetically trapped and do not undergo a magnetostructural transition. This is a dramatic example of the modification of a material's structural and magnetic properties at the nanoscale.

RESULTS AND DISCUSSION

Discrete nanoparticles of MnAs were prepared from arrested precipitation reactions using either a slow-heating method (method A, yielding type-A particles) or a high-temperature rapid-injection method (method B, yielding type-B particles).[10] Electron micrographs of the particles are shown in Figure 2, along with a size-distribution histogram. Type-A nanoparticles are faceted with a size of 22.3 ± 3.9 nm (measured along the shortest dimension), and type-B nanoparticles are slightly smaller, at 17.8 ± 3.1 nm. The aggregation observed in type-B MnAs particles revealed in the TEM image is not a universal phenomenon for nanoparticles of type-B MnAs[10] and may be a consequence of surfactant loss due to vigorous washing.

Examples of typical total scattering powder diffraction patterns in the form of PDFs are shown in Figure 3. We first verify that our results for the structure of the bulk material are in agreement with the literature;[4] that is, just below room temperature the samples are in the α phase and at just above room temperature in the β phase. In Figure 3a, we see a good agreement between the best-fit α model and the bulk MnAs data at 295 K, as additionally indicated by the low R_w (0.096).

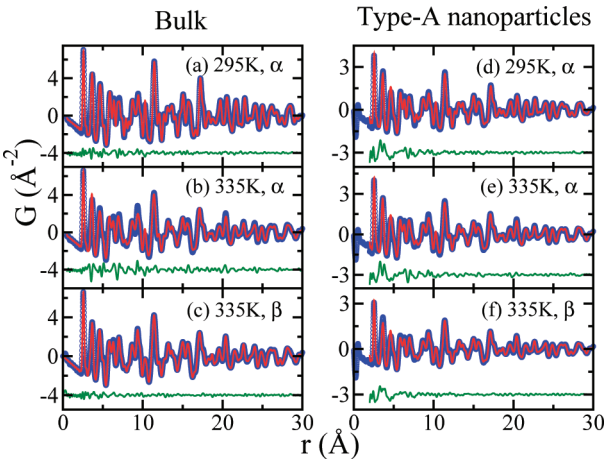

Figure 3. PDF refinements on bulk (left) and type-A nanoparticle (right) MnAs data. For each subfigure, the bulk circles represent the PDF from the experimental data and the red solid line is the calculated PDF after refinement. The green curve offset below is the difference curve between data and model.

TABLE 1. Refined Structural Parameters for Bulk and Type-A Nanoparticles at 295 and 335 K Using α (*P6$_3$mc*) and *β* (*Pnma*) Model[a]

		bulk		type-A nanoparticles	
parameter		295 K α	335 K *β*	295 K α	335 K *β*
a (Å)		3.724(2)	5.734(3)	3.686(5)	5.728(4)
b (Å)		3.724(2)	3.684(3)	3.686(5)	3.686(5)
c (Å)		5.712(5)	6.378(4)	5.731(13)	6.379(9)
Mn	*X*		0.0021(2)		0.0063(5)
	Z	−0.00014(9)	0.271(7)	0.009(2)	0.27(2)
	U_{iso} (Å^2)	0.014(3)	0.015(5)	0.021(12)	0.019(9)
As	*X*		0.231(7)		0.23(2)
	Z	0.25(2)	0.92(9)	0.24(3)	0.9(2)
	U_{iso} (Å^2)	0.009(2)	0.009(3)	0.013(9)	0.009(7)
R_w		0.096	0.084	0.203	0.189

[a] The refinable structural parameters are lattice parameters *a*, *b*, and *c*, Mn's *X* and *Z* fractional coordinates, As's *X* and *Z* fractional coordinates, and isotropic thermal factors U_{iso}.

Similarly, there is a good fit of the *β* model to the bulk data at 335 K as shown in Figure 3c and by an $R_w = 0.084$. For comparison, the best fit of the α model to the data at 335 K gives $R_w = 0.196$ and is shown in Figure 3b. The poor fit shows that the PDF is capable of differentiating between these phases. The refined values of the good fits are presented in Table 1. Our PDF refinements of the bulk are in excellent agreement with crystallographic results from the literature.[4]

We next consider type-A nanoparticles. In Figure 3d−f we show the fits of the bulk structural models to the PDFs of the type-A nanoparticles. The fits are good overall, indicating that these nanoparticles have similar structures to the bulk material. For the 335 K data (Figure 3e,f) the fit of the *β* structural model is better than the α model, as in the bulk. $R_w = 0.189$ for the *β* model and $R_w = 0.217$ for the α model, and the improved fit is evident by comparing the difference curves of (e) and (f) in Figure 3. However, the overall fit of the *β* model to the 335 K data is less good than for the bulk material. This is evident from the larger R_w (0.189 *vs* 0.084) and the clear features in the difference curves. This shows that there are structural modifications from the purely *β* structure in the nanoparticles, possibly from the surface region.

Figure 3d shows the fit of the α model to the type-A nanoparticle data collected at 295 K. There is a good overall fit, but the $R_w = 0.203$ is somewhat high, and there is some residual in the difference curve in Figure 3. We also attempted to fit the data with a two-phase mixture of α and *β* models to see if these features in the residuals could be explained by such a coexistence. The fits were not stable and did not improve the agreement. We do not believe that a phase mixture can explain the disorder observed in the difference curves of the NP samples.

However, the *β* model fits the 295 K data better ($R_w = 0.187$). This could be because the structure is still in the *β* form at this temperature and the sample has not transformed. However, another possibility is that the structure has transformed to the α phase but the *β* structural model fits better because it has more refinable parameters (12 for *β* *vs* 9 for α). This is possible because the α phase is similar to *β* and can be obtained in a continuous manner from *β* by adding some symmetry elements and moving atoms onto special positions. Thus, the observation of a lower R_w is not sufficient to establish that the material is in the α phase, and we need to look further. In order to establish definitively whether a structural transition is taking place in the type-A nanoparticles similar to that in MnAs bulk, we consider the *change* in the PDF of the material as its temperature is reduced from 335 to 295 K, shown in Figure 4. The difference curve in Figure 4a shows the changes in the PDF of bulk MnAs due to the structural transition, and Figure 4b shows the same for

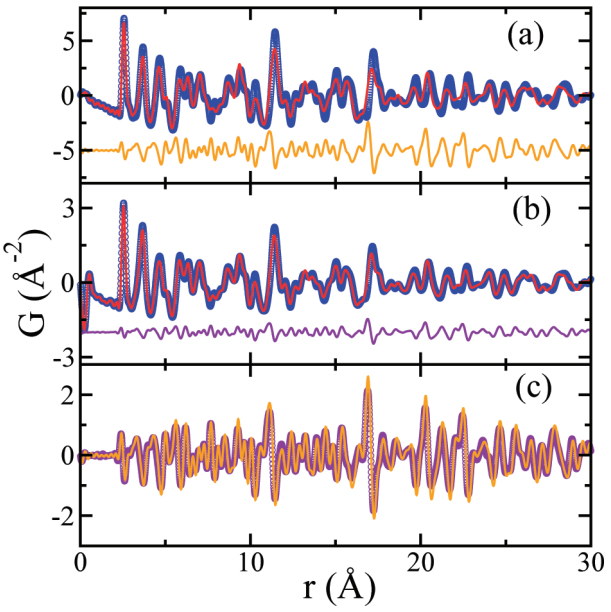

Figure 4. (a) Comparison of the difference (orange curve) between 295 (blue line) and 335 K (red line) PDF for bulk MnAs. (b) Same as (a) but for type-A nanoparticles with violet-colored difference curve. (c) Comparison of the difference curves from (a) and (b). The orange is the same as the difference curve in (a), and the violet is the result of scaling the curve in (b) by a factor of 4 for comparison. The analogous comparison based on diffraction patterns is available in the Supporting Information.

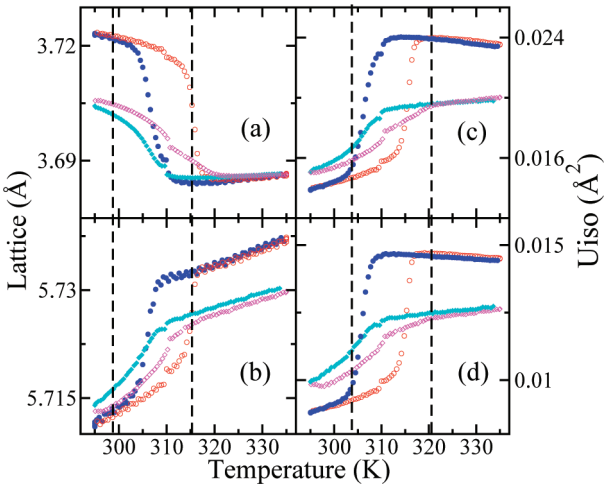

Figure 5. Lattice parameters (a, b) and atomic displacement factors (c, d) from PDF refinements on bulk and type-A samples using the α phase structure model. (a) and (b) are for lattice parameter *a* and *c* in units of Å. (c) and (d) are for U_{iso} of Mn and As in units of Å^2. For each subfigure, the blue and red are for bulk MnAs on the cooling and heating runs, respectively. The cyan and magenta are for type-A MnAs nanoparticles on cooling and heating runs, respectively.

the type-A nanoparticles. It is clear that the structural changes in the nanoparticles are smaller than those in the bulk. However, close inspection of the difference curves in Figure 4a and b shows that they are highly correlated and have similar features. To test the degree of correlation, we plot the two difference curves on top of each other in Figure 4c, multiplying the curve from the nanoparticles by a factor of 4 to account for the smaller amplitude of those changes. On the basis of the data in Figure 4c, we calculate the Pearson correlation coefficient[15,16] to show the degree of correlation between two difference curves. The value of the correlation can fall in the range from 1 (fully correlated) to −1 (anticorrelated), with the middle value, zero, meaning there is no correlation. For our case, the Pearson correlation coefficient between the two difference curves is 0.959, which clearly shows that the structural changes between 335 and 295 K of the bulk and type-A nanoparticles are the same. Thus, the type-A nanoparticles are undergoing the same structural phase transition as the bulk, although the amplitude of the changes is less.

Having established that the type-A nanoparticles are undergoing the same transition as the bulk, we next sought to compare the evolution of the transition with temperature and measure the structural hysteresis

TABLE 2. Refined Structural Parameters for Type-B Nanoparticles at 295 and 335 K Using the α (*P6₃mc*) and *β* (*Pnma*) Models[a]

parameter		295 K α	295 K *β*	335 K α	335 K *β*
a (Å)		3.669(6)	5.702(3)	3.675(6)	5.713(3)
b (Å)		3.669(6)	3.664(4)	3.675(6)	3.672(5)
c (Å)		5.719(12)	6.344(9)	5.724(11)	6.356(9)
Mn	*X*		−0.0023(3)		−0.0011(2)
	Z	0.008(2)	0.224(12)	0.008(7)	0.227(13)
	U_{iso} (Å^2)	0.03(2)	0.018(16)	0.03(2)	0.019(16)
As	*X*		0.27(7)		0.27(7)
	Z	0.24(3)	0.91(2)	0.24(3)	0.91(2)
	U_{iso} (Å^2)	0.017(14)	0.009(7)	0.016(13)	0.009(5)
R_w		0.305	0.201	0.275	0.197

[a] All parameters are the same as defined in Table 1.

curves of the two samples. The changes in *a* and *c* lattice parameters and in U_{iso} for Mn and As of bulk and type-A samples are shown in Figure 5. The hysteresis curves are very similar between the bulk and the type-A nanoparticles. For example, on cooling, the onset temperature of the structural transition is very similar. However, the hysteresis curves of the nanoparticles are less square than those of the bulk, and the size of the structural modifications (for example, the change in lattice parameters) is smaller in the nanoparticles. We conclude that the structural responses of the type-A nanoparticles are very similar to the bulk in most respects, but of a smaller magnitude, and the transition is smeared out in temperature on the low-*T* side. This transition broadening may be expected due to finite size effects of the nanoparticles.

The behavior of the type-B nanoparticles is very different. Structural results from representative temperature points are presented in Table 2. Figure 6c and d show the fits of the α and *β* structural models to the type-B nanoparticle PDFs at 335 K. The *β* model provides a better fit to the data and a lower R_w (0.197 *vs* 0.275), suggesting that at high temperature the material is in the *β* phase. However, as is the case for the type-A nanoparticles, the fit is far from ideal, suggesting additional structural relaxations. Also as with the type-A nanoparticles, attempts to fit the data with a mixed phase model of α and *β* together were unsuccessful. Figure 6a and b show the fits of the two structure models to the 295 K data. The *β* model provides a better fit than the α model (R_w = 0.201 and 0.305, for *β* and α models, respectively), which suggests that the structural transition may have been suppressed in these nanoparticles. As with the type-A nanoparticles, we test this hypothesis by looking at the change in the PDF between 335 and 295 K for the type-B nanoparticles and compare it to the bulk. The result is shown in Figure 7. The first observation is that the overall changes in the PDFs of the type-B nanoparticles are very small. The changes are comparable to the noise, with some small features that might be explained by a small change in lattice parameter due to thermal expansion. However, there is no indication of any structural phase transition on cooling for these samples. To make sure there is not a smaller magnitude phase transition as was observed in the type-A nanoparticles, we again look for correlations in the difference curves between 335 and 295 K compared to the bulk, which are plotted on top of each other in Figure 7c, after scaling up the type-B difference curve by a large factor of 10, in order to match the amplitude of the fluctuations. Visually there is no evidence of correlation, and the Pearson correlation coefficient is −0.197, which indicates the difference curves are essentially uncorrelated. This result indicates that the structural transition has been completely suppressed in the type-B nanoparticles. Furthermore, plots of the temperature dependence of the structural parameters from type-B nanoparticles (not shown) do not show hysteresis similar to those of the bulk and type-A nanoparticles. Interestingly, the unit cell volume of the type-B nanoparticles is significantly less than the bulk or the type-A nanoparticles as shown in Figure 8b. For example, the cell volume is decreased by 0.89% at 335 K and by 2.71% at 295 K compared to the bulk. This synthesis method has clearly produced nanoparticles that, although similar in size and composition, are structurally distinct.

Finally, we would like to establish the relationship between the magnetic and structural transitions. This comparison is shown in Figure 8. In agreement with the literature[4] we see a strong correlation between the structural and magnetic transitions in the bulk, as can be seen by comparing the red and blue curves in Figure 8a (magnetic) and 8b (structural), where the structural parameter we choose to plot is the unit cell volume. The cyan and magenta curves show the same comparison for the type-A nanoparticles. Again, the magnetic and structural transitions appear to be coupled, although the hysteresis in the magnetic data is far smaller than that observed in the structural data. The increase in the magnetization on cooling is decreased in the type-A nanoparticles, relative to the bulk, and this correlates to a smaller increase in cell volume. Most significantly, the width of the thermal hysteresis in the magnetization is much smaller for the type-A nanoparticles, on the order of only 1 K, than for the bulk sample, close to 10 K. This is observed despite the structural hysteresis being broader in the nanoparticles than in the bulk. Thus, the structural and magnetic transitions are related, but not completely dependent on each other.

The volume of the type-A nanoparticles in the low-spin *β* phase is the same as for the bulk material, although the increase in the volume on entering the α phase is less, consistent with the decreased magnetization in that phase. The small suppression in the magnetic signal can perhaps be attributed to surface effects in the nanoparticle sample. This suggestion is

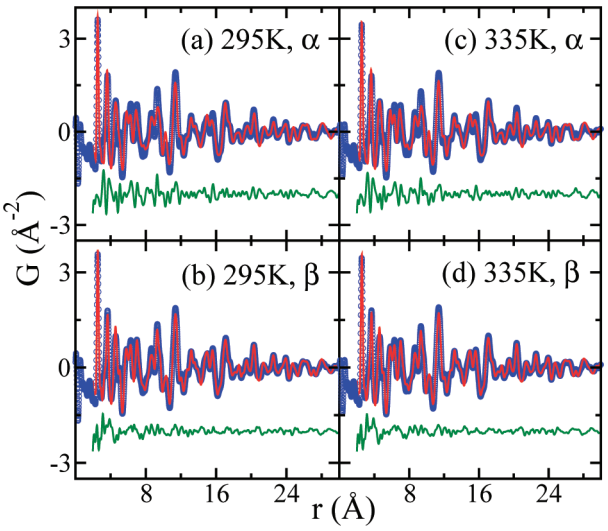

Figure 6. PDF refinements on data acquired on type-B nanoparticles at 295 (a, b) and 335 K (c, d) using the α (a, c) and β (b, d) phase model, respectively. For each subfigure, the symbol and color representations are the same as in Figure 3.

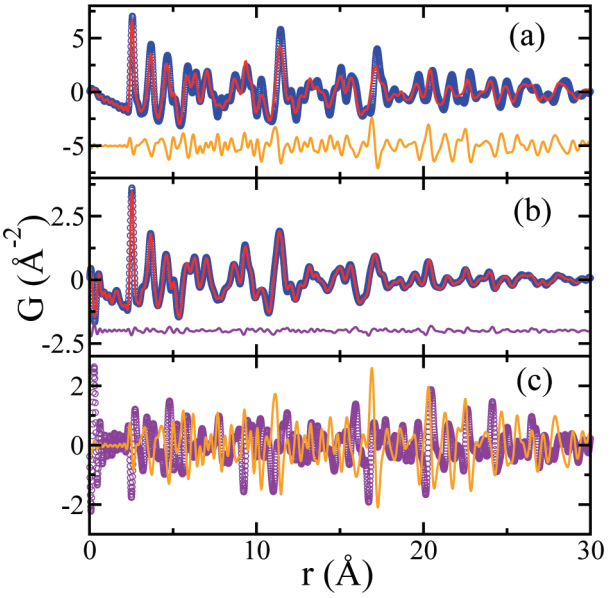

Figure 7. Same as Figure 4 but for type-B nanoparticles. In (c) the difference curve (violet) of type-B nanoparticles is scaled by a factor of 10 since its amplitude is too small to compare with the bulk one. The analogous comparison based on diffraction patterns is available in the Supporting Information as well.

supported by the observation that the high temperature susceptibility in the type-A nanoparticles is smaller than that of the bulk sample, so that the relative change in magnetic susceptibility, $\chi'(T=295\text{K}) - \chi'(T=335\text{K})/\chi'(T=335\text{K})$, is approximately equal. These measurements support the conclusion that the magnetostructural transition in the type-A nanoparticles is qualitatively similar to that occurring in bulk MnAs, but involving a smaller amount of distortion.

The temperature dependence of the magnetic susceptibility for the type-B nanoparticles, also plotted in Figure 8, differs strikingly from the behavior of the type-A nanoparticles and bulk MnAs. The type-B nanoparticles have a negligible magnetic susceptibility at 335 K, consistent with a weakly paramagnetic low-spin state. There is a small, but distinct increase in susceptibility at lower temperatures. This transition can be seen most clearly in the data collected on warming, which suggest a transition from a weakly ferromagnetic to paramagnetic state at a temperature similar to what is observed in the type-A nanoparticles. In addition to the magnitude of the susceptibility being greatly suppressed from that of the type-A nanoparticles, the thermal hysteresis in the susceptibility is also much broader for the type-B nanoparticles, extending over at least 30 K. The fact that the susceptibility in the type-B nanoparticles is a significant fraction of that found in the type-A nanoparticles together with the

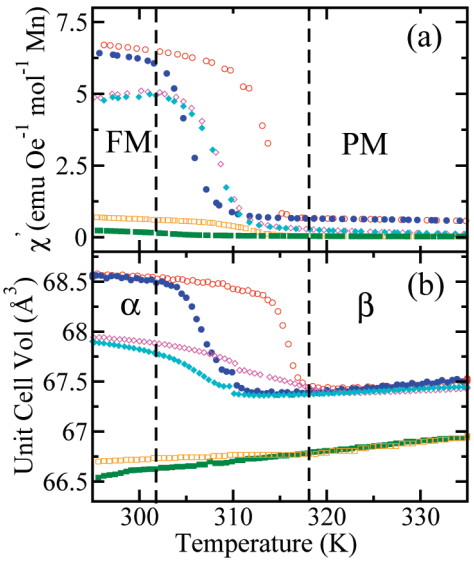

Figure 8. Real part of the ac magnetization (a) and unit cell volume (b) in bulk and type-A and type-B nanoparticles. All of the unit cell volumes are based on the results of α-model refinements. The blue (cooling) and red (heating) are for the bulk sample, cyan (cooling) and magenta (heating) are for type-A nanoparticles, and the green (cooling) and orange (heating) are for type-B. The dashed lines at 303 and 317 K show the temperature range of the structural transitions in bulk MnAs as reported in the literature.[4]

different temperature dependence of the two samples makes it unlikely that the magnetic response in the type-B nanoparticles arises from some type-A impurity that was not detected by our other techniques.

This magnetic transition in the type-B nanoparticles does not appear to be linked to a structural transition but may be connected to an observed irreversibility in the unit cell volume on cooling. This evidence for a magnetic transition in the type-B nanoparticles in the absence of any clear structural transition suggests that the interplay between magnetism and crystal structure in MnAs may be more complex than previously believed.

The type-B nanoparticles are smaller than the type-A. An interesting question is whether their very different structures and properties are due to the smaller size or the different synthesis method. Here we argue that the prime factor is the synthesis method. We have made type-B nanoparticles with sizes up to 26 nm, and these behave the same way as the smaller type-B nanoparticles studied here. Thus, the fact that the type-B nanoparticles are smaller than type-A in the present case is not the dominant factor governing phase stability.

CONCLUSION

Structurally distinct samples of MnAs nanoparticles have been prepared using either slow-heating (method A) or high-temperature rapid-injection (method B) arrested precipitation reactions, and their temperature-dependent structures and magnetic characteristics have been probed. Using Rietveld and PDF methods, we confirm that the structure transition in bulk MnAs is highly correlated with the magnetic transition, as previously reported. Type-A nanoparticles have a similar structural transition that happens in the same temperature region as bulk, but the changes are smaller in amplitude. Once again, a clear magnetic transition correlates with what is happening structurally. This is in contrast to previous reports wherein no structural transformation was observed for type-A nanoparticles by traditional temperature-dependent powder X-ray diffraction methods, despite the persistent observation of a magnetic transition[10] and highlights the sensitivity of the PDF approach in probing structural transformations in nanoscale materials. Type-B nanoparticles are distinct from both the bulk and type-A nanoparticles, adopting the β structure over the entire temperature range. The fact that type-A particles predictably cycle between α and β, whereas type-B nanoparticles are kinetically trapped, suggests the structure is pinned, possibly by impurity ion inclusion during the rapid nucleation inherent in the method B synthesis. Previous studies have demonstrated a slow conversion over time to the thermodynamic α phase. Partial conversion during the data acquisition could explain some of the irreversibility observed in both the structural and magnetic data. A detailed study of the kinetic stability of type-B nanoparticles as a function of particle size is underway.

METHODS

Synthesis. The bulk MnAs we used for this study was purchased from Pfaltz and Bauer Chemicals. A chemical etching process was performed to eliminate impurities. Briefly, 1 g of ground bulk MnAs was combined with 20 mL of concentrated HCl solution, slowly heated to 80 °C, and kept at that temperature for 20 min. The sample was then washed with 50 mL of deionized water several times to remove the soluble impurities.

The synthesis of MnAs nanoparticles can be achieved by either a slow-heating method or a high-temperature fast-injection method. We call these approaches method A and method B, respectively. The resulting nanoparticles are called type-A and type-B. In method A, 0.256 mmol of $Mn_2(CO)_{10}$ is combined with 0.528 mmol of $Ph_3As{=}O$, 8.0−10.0 mL of 1-octadecene, and 5 g of trioctylphosphine oxide (TOPO) in a Schlenk flask under argon. The mixture is gradually heated to 250 °C over 2 h, changing from yellow to orange to black, and then maintained at this temperature for 18 h. The as-prepared nanoparticles are then isolated by centrifugation after dispersing in chloroform and precipitating in absolute ethanol. This dispersion/reprecipitation process is repeated several times to ensure complete removal of TOPO and reaction byproducts.

For method B, the fast-injection method, the same amount of $Mn_2(CO)_{10}$, $Ph_3As{=}O$, and 1-octadecene are combined together in a Schlenk flask under argon. The mixture is heated slightly using a heatgun until the powder precursors are dissolved. This mixture is then cannulated under inert

conditions into hot TOPO (5.0 g) maintained at 330 °C in a second Schlenk flask. The reaction is maintained at 330 °C for 18 h. The nanoparticles are isolated using the procedure described for type-A MnAs.

Particle size and morphology were assessed using transmission electron microscopy studies performed on a JEOL 2010 HRTEM operating at 200 kV. Samples were prepared by dispersion of solid precipitates in chloroform, and then a drop of the colloidal solution was deposited on a carbon-coated copper grid and allowed to air-dry.

Diffraction Experiments. Total scattering powder diffraction experiments were performed at the 11-ID-B beamline at the Advanced Photon Source at Argonne National Laboratory, with 58.26 keV X-rays using the rapid acquisition (RaPDF) mode.[16] A large area 2D GE Revolution 41RT flat panel detector[17] was mounted orthogonal to the beam path. Each sample was packed in a kapton capillary 1 mm in diameter and measured in the temperature range 295−335 K during heating and cooling. In the heating (cooling) procedure we continuously increase (decrease) the temperature at 1 K/min rate and collect data frames every 30 s, *i.e.*, every 0.5 K. In the measured range 295−335 K, this results in ∼80 data sets for both the heating and cooling runs. The raw 2D data were integrated and converted to intensity *versus* 2θ using the software Fit2D,[18] where 2θ is the diffraction angle.

Rietveld refinements were carried out on the data using the GSAS[19] and FullProf[20] programs controlled by the SrRietveld program.[21] SrRietveld is a highly automated program for Rietveld refinement. It not only can do the conventional refinement by using GSAS and FullProf as the engines but also can automate the refinement of large numbers of data sets with minimal human effort. As the first step of the Rietveld refinement, instrument parameters were calibrated using standard silicon data. There are two structural models for the MnAs samples: the α phase model in the *P*63*mc* space group and the β phase model in the *Pnma* space group. The refinable structural parameters were *a*, *b*, and *c*, Mn's *X* and *Z* fractional coordinates, As's *X* and *Z* fractional coordinates, and isotropic thermal factors on each symmetry-independent atomic site. The peak profile used was the Thompson−Cox−Hastings pseudo-Voigt function (CW profile function 2 in GSAS and Npr=7 in FullProf). The background function used was a Chebyschev polynomial in GSAS and linear interpolation in FullProf. The refinement strategy used was to turn on scale factor, then zero shift, background coefficients, lattice parameters, peak profile parameters, all allowed atom fractional coordinates, and finally, isotropic thermal factors.

The PDF, $G(r)$, was obtained by Fourier transformation of the reduced total scattering structure $F(Q) = Q(S(Q) - 1)$ according to eq 1.[11]

$$G(r) = \frac{2}{\pi}\int_{Qmin}^{Qmax} Q[S(Q) - 1]\sin Qr\, dQ \qquad (1)$$

where $S(Q)$ is obtained from a diffraction experiment. The maximum range of Q used in the Fourier transform was Q_{max} = 23.0 Å^{-1}. The value of Q_{max} chosen to optimize the PDF was selected by choosing the largest Q_{max} possible without introducing too much statistical noise into the data. The PDFs were modeled using PDFgui.[22] The structural models and refinable parameters are the same as Rietveld refinement discussed above, but the PDF refinements yield information about the local structure rather than the average crystal structure probed by Rietveld refinement. Because of the relatively large size[14] of the nanoparticles in this study, the results from average and local structural refinements matched each other well for all the MnAs samples, and so, for the sake of brevity, we present only the PDF results in this paper.

Magnetization Measurements. Ac magnetic susceptibility measurements, which are more sensitive to small changes in magnetization arising from possible impurity phases than dc measurements, were carried out at 10 kHz using a standard option on a Quantum Design Physical Properties Measurement System. The magnetic susceptibility was measured on heating and cooling from 280 to 340 K at an ac excitation field of 10 Oe with zero dc field. Bulk, type-A, and type-B MnAs nanoparticles were prepared by sealing loose powders in evacuated quartz tubes. The data were normalized to total Mn quantity based on chemical analysis data acquired by atomic absorption spectroscopy using a Perkin-Elmer Analyst 700 instrument. Solid samples were dissolved in nitric acid, diluted, and compared to a calibration curve created using a series of Mn standards (high-purity standards).

Acknowledgment. We thank P. Juhas, C. Farrow, and E. Bozin for assistance with the experimental setup and data collection. Work in the Billinge group was supported by the National Science Foundation (NSF) through grant DMR-0703940. Work in the Brock group was supported by NSF through grant DMR-0701161. Work in the Lawes group was supported by the NSF through grant DMR-0644823. The APS at Argonne National Laboratory is supported under DOE contract No. DE-AC02-06CH11357.

Supporting Information Available: Diffraction data analogous to PDF data shown in Figures 4 and 7. This material is available free of charge *via* the Internet at http://pubs.acs.org.

REFERENCES AND NOTES

1. Mira, J.; Rivadulla, F.; Rivas, J.; Fondado, A.; Guidi, T.; Caciuffo, R.; Carsughi, F.; Radaelli, P. G.; Goodenough, J. B. Structural Transformation Induced by Magnetic Field and "Colossal-Like" Magnetoresistance Response above 313 K in MnAs. *Phys. Rev. Lett.* **2003,** *90*, 097203.
2. Ranke, P. J. V.; Gama, S.; Coelho, A. A.; de Campos, A.; Carvalho, A. M. G.; Gandra, F. C. G.; de Olivera, N. A. Theoretical Description of the Colossal Entropic Magnetocaloric Effect: Application to MnAs. *Phys. Rev. B* **2006,** *73*, 014415.
3. Zou, J. D.; Wada, H.; Shen, B. G.; Sun, J. R.; Li, W. Giant Magnetocaloric Effect and Soft-Mode Magneto-Structural Phase Transition in MnAs. *Phys. Rev. B* **2008,** *81*, 47002.
4. Rungger, I.; Sanvito, S. Ab Initio Study of the Magnetostructural Properties of MnAs. *Phys. Rev. B* **2006,** *74*, 024429.
5. Mosca, D. H.; Vidal, F.; Etgens, V. H. Strain Engineering of the Magnetocaloric Effect in MnAs Epilayers. *Phys. Rev. Lett.* **2008,** *101*, 125503.
6. Gama, S.; Coelho, A. A.; de Campos, A.; Carvalho, A. M. G.; Gandra, F. C. G.; Ranke, P. J. V.; de Olivera, N. A. Pressure-Induced Colossal Magnetocaloric Effect in MnAs. *Phys. Rev. Lett.* **2004,** *93*, 237202.
7. Bean, C. P.; Rodbell, D. S. Magnetic Disorder as a First-Order Phase Transformation. *Phys. Rev.* **1962,** *126*, 104–115.
8. Takagaki, Y.; Herrmann, C.; Wiebicke, E.; Herfort, J.; Daweritz, L.; Ploog, K. H. Slow Relaxation of Magnetization in MnAs Nanomagnets on GaAs(001). *Appl. Phys. Lett.* **2006,** *88*, 032504.
9. Ramlan, D. G.; May, S. J.; Zheng, J. G.; Allen, J. E.; Wessels, B. W.; Lauhon, L. J. Ferromagnetic Self-Assembled Quantum Dots on Semiconductor Nanoparticles. *Nano Lett.* **2006,** *6*, 50–54.
10. Senevirathne, K.; Tackett, R.; Kharel, P. R.; Lawes, G.; Somaskandan, K.; Brock, S. L. Discrete, Dispersible MnAs Nanocrystals from Solution Methods: Phase Control on the Nanoscale and Magnetic Consequences. *ACS Nano* **2009,** *3*, 1129–1138.
11. Egami, T.; Billinge, S. J. L. *Underneath the Bragg Peaks: Structural Analysis of Complex Materials*; Pergamon Press, Elsevier: Oxford, England, 2003.
12. Billinge, S. J. L. Nanoscale Structural Order from the Atomic Pair Distribution Function (PDF): There's Plenty of Room in the Middle. *J. Solid State Chem.* **2008,** *181*, 1698–1703.
13. Neder, R. B.; Korsunskiy, V. I. Structure of Nanoparticles from Powder Diffraction Data Using the Pair Distribution Function. *J. Phys.: Condens. Matter* **2005,** *17*, S125–S134.
14. Masadeh, A. S.; Božin, E. S.; Farrow, C. L.; Paglia, G.; Juhás, P.; Karkamkar, A.; Kanatzidis, M. G.; Billinge, S. J. L. Quantitative Size-Dependent Structure and Strain Determination of CdSe Nanoparticles Using Atomic Pair Distribution Function Analysis. *Phys. Rev. B* **2007,** *76*, 115413.

15. Myers, J. L.; Well, A. D. *Research Design and Statistical Analysis*, 3rd ed.; Lawrence Erlbaum Associates: Hillsdale, 2010.
16. Chupas, P. J.; Qiu, X.; Hanson, J. C.; Lee, P. L.; Grey, C. P.; Billinge, S. J. L. Rapid Acquisition Pair Distribution Function Analysis (RA-PDF). *J. Appl. Crystallogr.* **2003,** *36*, 1342–1347.
17. Chupas, P. J.; Chapman, K. W.; Lee, P. L. Applications of an Amorphous Silicon-Based Area Detector for High-Resolution, High-Sensitivity and Fast Time-Resolved Pair Distribution Function Measurements. *J. Appl. Crystallogr.* **2007,** *40*, 463–470.
18. Hammersley, A. P.; Svenson, S. O.; Hanfland, M.; Hauserman, D. Two-Dimensional Detector Software: from Real Detector to Idealised Image or Two-Theta Scan. *High Pressure Res.* **1996,** *14*, 235–248.
19. Larson, A. C.; Von Dreele, R. B. Report No. LAUR-86-748; Los Alamos National Laboratory: Los Alamos, NM 87545.
20. Rodriguez-Carvajal, J. Recent Advances in Magnetic Structure Determination by Neutron Powder Diffraction. *Phys. B (Amsterdam, Neth.)* **1993,** *192*, 55–69.
21. Tian, P.; Zhou, W.; Liu, J.; Shang, Y.; Farrow, C. L.; Juhás, P.; Billinge, S. J. L. SrRietveld: A Program for Automating Rietveld Refinements for High Throughput Studies. *arXiv* 2010, arXiv:1006.0435.
22. Farrow, C. L.; Juhás, P.; Liu, J.; Bryndin, D.; Božin, E. S.; Bloch, J.; Proffen, T.; Billinge, S. J. L. PDFfit2 and PDFgui: Computer Programs for Studying Nanostructure in Crystals. *J. Phys: Condens. Matter* **2007,** *19*, 335219.